Chapter 4: Structure and transformations of bcc elemental metal clusters

4.1 Introduction

Determination of the crystallography of clusters is an important step in the process of understanding the functionality of clusters. For transition metal clusters, numerous experiments have been performed dealing with chemical reactivity, but results on the specific geometrical structure are relatively few. Those that have been obtained are mainly concerned with small clusters of tens to a few hundreds of atoms [1]. Here, the peaks observed in mass spectra are consistent with the completing of successive geometric shells of atoms. This type of measurement can be difficult to perform for larger clusters, due to the limited detection range of mass spectrometers, or because not all cluster sources are effective at producing heavier clusters.

In general, the crystal structure and crystal habit of nanoclusters depend on their composition and temperature [2]. In many cases clusters have the form of polyhedra with varying degrees of truncation. These shapes occur either in order to minimize the surface energy, or because of the kinetics of growth. If kinetics dominates, then the shape is determined by the nucleation rate and the rate at which different crystal faces grow. If, on the other hand, the clusters are formed in thermal equilibrium, their shape or crystal habit results from minimizing the surface energy. In this case, the shape can be determined by applying a Wulff construction. For many body-centered cubic (bcc) elements, including Fe, V, Nb, Cr, and Mo, the nanoclusters often have the shape of a truncated rhombic dodecahedron [2]. Furthermore, the atomic arrangement of these elements can transform to face-centered cubic (fcc) below a certain cluster size, in order to lower the surface energy [3].

The large surface area of nanoclusters can also make them highly reactive. Thus, it is not surprising that metallic nanoclusters are sometimes coated with an oxide layer, or even completely oxidized when they are exposed to air. An oxidation process may be stimulated by temperature or by irradiation with an electron beam. Heating of the clusters is likely to induce other transformations as well, such as coalescence and changes in shape. In this chapter, the crystallography and other structural properties of nanosized clusters of several bcc elements (Fe, Nb, Mo) are explored by means of transmission electron microscopy (TEM).

Transmission electron microscopy is a very suitable technique to analyze nanoscale clusters and materials based on these clusters. Two microscopes used in the present

work are a JEOL 4000 EX/II having a point-resolution of 0.17 nm, and a JEOL 2010F with an information limit of 0.11 nm. Their maximum accelerating voltages are 400 kV and 200 kV, respectively, and the corresponding electron wavelengths 1.9×10^{-3} nm and 2.5×10^{-3} nm. The JEOL 2010F has the capability to form an electron probe with a minimum diameter of 0.5 nm, allowing chemical analysis (energy-dispersive X-ray spectroscopy and parallel electron energy loss spectroscopy) with a spatial resolution currently not attainable by any other instrument than a field-emission gun TEM.

Cluster sizes and shapes (faceting) and the corresponding distributions can be imaged directly, i.e., in real space. The crystalline or amorphous structure within the nanoclusters, potentially with defects, can be unraveled. An important issue is the difference in contrast between the nanoclusters and e.g. the amorphous carbon used as support. For the same thickness, crystalline phase gives more contrast than amorphous phase, and the higher the atomic weight of the clusters, the stronger the difference in contrast with the carbon. For use within the 2010F a double-tilt heating stage (up to 1000°C) is available allowing *in situ* analysis of the effects of annealing. This provides valuable information about the response of cluster-assembled materials to high temperatures, specifically about their growth and sintering behavior.

4.2 Deposition and analysis of iron clusters

Iron clusters were produced from an electrolytically pure sputtering target (99.98% Fe). The target was machined to a thickness of 0.8-0.9 mm, after initial tests with 2.2 mm thickness produced only a faint and unstable plasma discharge. A magnetic material can interfere with the field of the magnetron; an effect that is minimized by using a thinner target (see also Section 2.7). The base pressure was $\sim10^{-8}$ mbar, both in the differential pumping stage and the substrate chamber. Sputtering took place under an Ar atmosphere of ~0.07 mbar, while helium was supplied to the aggregation zone via the drift gas inlet. The partial pressure of helium was an order of magnitude lower than for argon. We found that adding helium increases the cluster deposition rate which is otherwise very low for iron. The main purpose of helium is to enhance the transport efficiency and thus reduce the growth time of clusters (Section 2.9); in this case it also resulted in a higher number of clusters arriving at the substrate, although it was still far below the deposition rate for copper (fig. 4.1). Various deposition experiments were performed with magnetron voltages ranging from 250 to 400 V, and plasma currents around 0.26 A. Clusters were directly deposited onto support films of silicon nitride or carbon (20 nm thickness) before analysis in the JEOL2010F microscope.

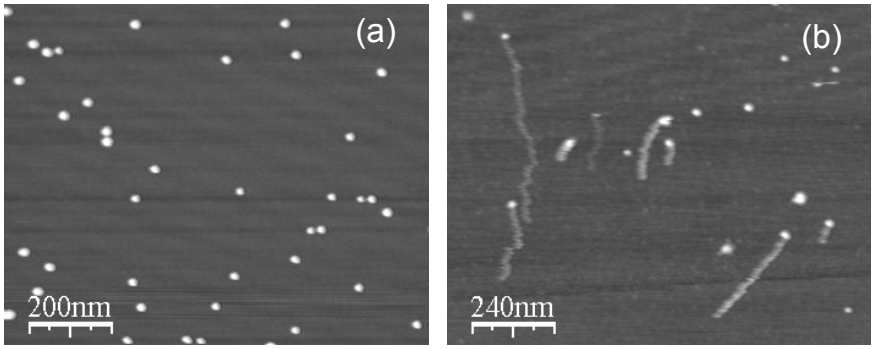

Figure 4.1: (a) *Fe clusters deposited on silicon, AFM image.* **(b)** *Another Fe sample imaged by AFM, showing trails formed during scanning.*

Figure 4.1(a) is a typical AFM image of Fe clusters on a Si(100) surface, obtained after 5 min deposition with an Ar/He gas mixture. The clusters appear as isolated features that are randomly scattered across the plane, indicating a rather strong interaction between the clusters and the surface. Indeed, deposition onto a reactive surface such as Si(100) is an effective way to limit the diffusion of clusters [4]. However, in a few cases we found evidence that clusters would move under the influence of an AFM tip. The image in Fig. 4.1(b) was taken on another sample prepared under similar conditions. The AFM settings were similar as well, apart from a higher tip velocity (12 μm/s versus 4 μm/s). Apparently, some clusters move a small distance each time that the tip passes, in roughly the same direction as the slow scan axis ("up" in Fig. 4.1(b)). This eventually leads to trails that do not represent actual topographic features of the sample. The fact that Fe clusters can be manipulated in the dynamic AFM mode, where tip-sample interactions are inherently low, indicates that they are not as strongly bound to the surface as expected.

A TEM image of deposited iron clusters (Fig. 4.2(a)) demonstrates the uniformity in cluster size, with an average diameter of about 10 nm. Closer examination revealed that an oxidation process took place while the sample was exposed to air, during a quick transfer from the source to the transmission electron microscope. The result is exhibited in Figure 4.2(b), where a typical cluster consisting of an iron core of 5 nm diameter is enclosed in an iron oxide shell of approximately 2 nm thickness. By electron diffraction analysis, as well as lattice spacing measurements on the metallic core, we verified that the crystal structure corresponded to bcc iron. However, the original cluster shape is probably altered as a result of oxide formation. Figure 4.2(c) shows how the crystal structure of an Fe cluster is modified after prolonged exposure to the intense electron beam (200 kV) – the observed fringes no longer correspond to the bcc structure.

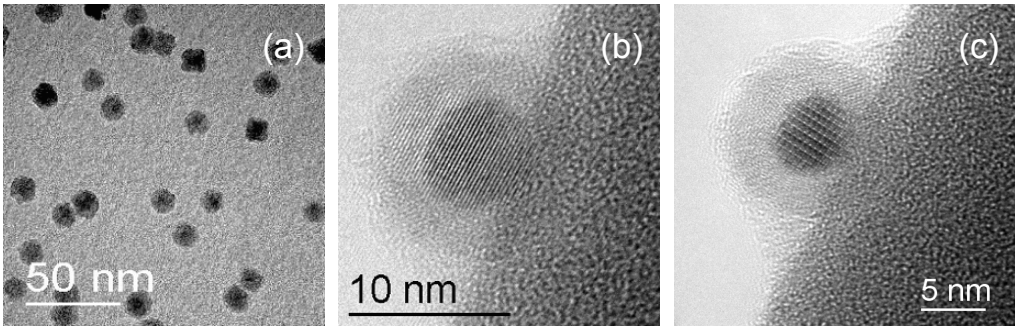

Figure 4.2: (a) *Transmission electron micrograph of Fe nanoclusters deposited on Si_3N_4 membrane.* **(b)** *TEM micrograph of a single Fe cluster briefly exposed to air. Lattice fringes correspond well with {110} planes of bulk α- iron.* **(c)** *The same cluster as in (b) after longer irradiation with the electron beam, showing modified internal structure.*

Various possibilities exist for the type of oxide: γ-Fe_2O_3, which is the most abundant form of iron oxide, or alternatively, the Fe_3O_4 phase. Dupuis et al. [5], who studied iron thin films composed of 2-6 nm clusters produced in a laser vaporization source, found that 20% of their sample material had been converted to both Fe_3O_4 and γ-Fe_2O_3. The oxidation of iron requires addition of oxygen to the cluster, which results in an increase of the cluster size [4]. However, the shell of oxide is thermally unstable due to its nanometer scale thickness, and it does not resist even moderate annealing at temperatures around 500°C.

Structural evolution of the iron clusters was monitored during *in-situ* annealing at a pressure ~10^{-4} mbar. Clusters start to fuse around 500°C: neighboring clusters merge to form larger particles (Fig. 4.3), whereas isolated clusters stay intact and appear to be immobile. There is no evidence for surface diffusion of individual clusters. Note that these phenomena were observed far below the melting temperature of bulk iron: T_m=1538°C.

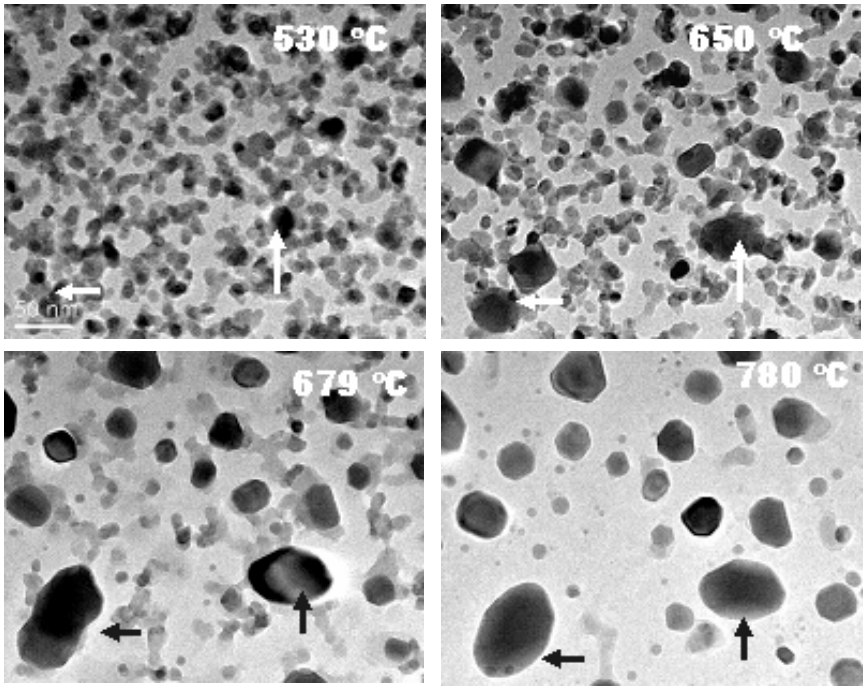

Figure 4.3: *Successive stages of the coalescence and growth of Fe nanoclusters during heating. Sequence is from top left to bottom right; temperatures are indicated.*

Figure 4.4 illustrates the decomposition of the oxide shell during annealing. An iron oxide phase is no longer detectable either by elemental mapping or by diffraction analysis. Nevertheless, the elemental map indicates that oxygen is present beyond the region occupied by a cluster (Fig. 4.4(b)); this is probably due to substrate oxidation. A sample drift during these measurements can be excluded by comparing the locations of the oxygen-rich areas (arrows) to those in the corresponding bright-field TEM image (Fig. 4.4(a)). After annealing and thermal break-up of the oxide shells, the crystal structure of the remaining clusters still remains bcc but they are characterized by distinctly facetted shapes (Fig. 4.5). In the following the crystal habit of these annealed clusters is discussed in more detail.

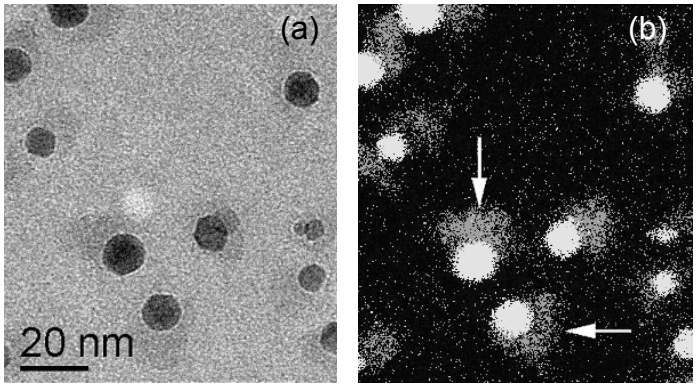

Figure 4.4: (a) *TEM bright field image, and* **(b)** *the corresponding elemental map made by means of energy filtered TEM. Arrows point to oxygen-rich areas (gray); bright areas contain iron. Oxygen was not detected at the sites occupied by clusters.*

The most stable structures for medium-sized clusters (i.e., 100-10000 atoms), calculated using an empirical many-body potential function [6], are the bcc rhombic dodecahedron with 12 pseudo-closepacked {110} faces (having the lowest surface energy for bcc structures), and the icosahedron which is favorable for smaller clusters. A transition from icosahedron to bcc rhombic dodecahedron is predicted for clusters of approximately 2000 atoms [6]. The rhombic dodecahedron is actually a fragment of the bcc lattice, in the same way that an icosahedron is a fragment of the fcc lattice. Other possibilities for stable iron clusters are the cuboctahedron (fcc) and the truncated decahedron, which could be feasible for clusters smaller than those in the present work [6].

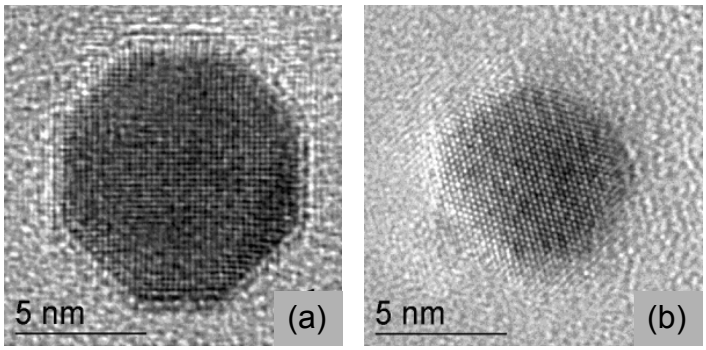

Figure 4.5: *Lattice imaging of two nanoclusters after in–situ annealing in TEM. Oxide shells have been disintegrated. The clusters are oriented with respect to the electron beam as follows:*
(a) *<100> bcc;* **(b)** *<111> bcc.*

Two typical clusters as observed after *in-situ* heat treatments are displayed in Figure 4.5. The octahedral contour in the <100> projection (Fig. 4.5(a)), in combination with the <111> projection as seen in Figure 4.5(b) , suggest that the cluster is shaped like a truncated rhombic dodecahedron, exposing twelve {110} faces, six {100} faces, and eight {111} faces. By truncation, a rhombic dodecahedron adopts a more spherical shape, but this also increases the area fraction of higher-energy faces on a bcc cluster. The degree of truncation can be measured by the ratio λ_2/λ_1 as illustrated in Fig. 4.6(a). When $\lambda_2/\lambda_1=0$, there is no truncation of the rhombic dodecahedron, while the case of $\lambda_2/\lambda_1=1$ corresponds to a fully truncated shape, i.e., a cuboctahedron (Fig. 4.6(b)).

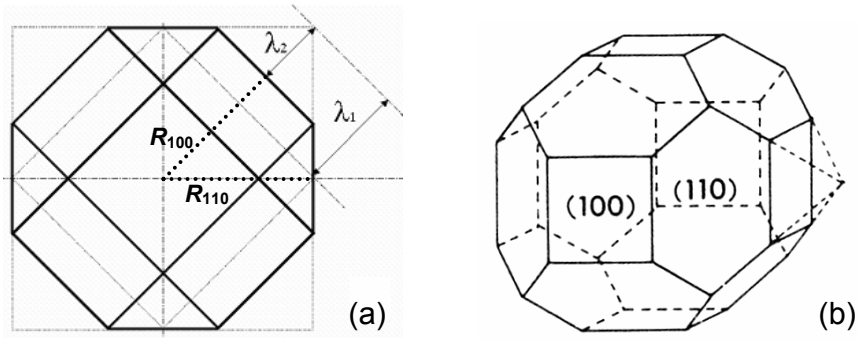

Figure 4.6: (a) *Drawing of the <100> projection of a truncated rhombic dodecahedron with schematic explanation of the truncation ratio* λ_2/λ_1. **(b)** *3D model a truncated rhombic dodecahedron [2]. Note that this is rotated over 45 degrees with respect to the first figure.*

An average experimental value of the λ_2/λ_1 ratio is 0.565±0.05. From this one can estimate the ratio of surface energies $\gamma_{100}/\gamma_{110}$, based on the Wulff construction which states that the distance of a surface plane from the center-of-mass is proportional to the surface energy of that plane. If we define R_{110} and R_{100} as the respective distances from the center of the polyhedron to the {110} and {100} faces (Fig. 4.6(a)), then the Wulff method assumes that $R_{110} \propto \gamma_{110}$ and $R_{100} \propto \gamma_{100}$. From this we obtain:

$$\frac{R_{100}}{R_{110}} = \frac{\gamma_{100}}{\gamma_{110}} \tag{4.1}$$

The truncation parameters λ_1 and λ_2 can be expressed in terms of R_{110} and R_{100} as:

$$\lambda_2 = \sqrt{2}R_{110} - R_{100}$$
$$\lambda_1 = \frac{1}{2}\sqrt{2}R_{110} \tag{4.2}$$

Calculating the truncation ratio from Eqs. (4.2), and substituting from Eq. (4.1), we obtain the result:

$$\frac{\lambda_2}{\lambda_1} = 2 - \sqrt{2}\frac{\gamma_{100}}{\gamma_{110}} \tag{4.3}$$

Thus, the observed truncation ratio of λ_2/λ_1=0.565 translates to a ratio of surface energies $\gamma_{100}/\gamma_{110}$=1.02. Note that true equilibrium shapes as predicted by the Wulff method are not often observed in reality, because a given crystal can have different morphologies depending on its history and its rate of growth in different directions. If other parameters than the surface energies are involved, then the above estimation may not be entirely accurate. Still, the result for $\gamma_{100}/\gamma_{110}$ is in reasonable agreement with surface energies calculated by Jiang et al. [7], which would predict a ratio $\gamma_{100}/\gamma_{110}$=1.13 for bcc Fe in bulk form. The truncation that we observed for re-formed clusters, either isolated or grown by fusion of smaller clusters, has not been predicted by theory [6]. A plausible reason is that the theoretical calculations concern static properties of free clusters at zero Kelvin, thus ignoring effects of temperature and cluster dynamics.

Summarizing the results for Fe clusters, we have shown that exposure to atmospheric conditions leads to oxidation, where the oxide takes the form of a 2 nm-thick shell surrounding the metallic core. The oxide shell was directly observed in the high-resolution imaging mode, whereas previous studies relied on Mössbauer spectra [5] or cluster volume measurements [4] to determine the extent of oxidation. Many structural and functional properties of clusters that are of interest require sample transfer through atmosphere with the risk of oxidation [4]. This could have significant consequences for Fe cluster-assembled materials, because the pure iron phase is magnetic while the oxide is nonmagnetic [5]. In addition, the behavior of the material at high temperatures is important, for example in devices where operation leads to heating and possible degradation of performance. In our in-situ annealing experiments, the iron oxide shell breaks down at around 500°C, and further heating results in fusion of clusters when they are initially in contact. Finally, the shape of Fe clusters after annealing corresponds to a truncated rhombic dodecahedron, which deviates from former calculations of stable structural forms [6].

4.3 Geometry and stability of niobium clusters

A niobium target was sputtered at ~240 V magnetron voltage and an ion current of 0.50 A (~120 W power). Argon gas was introduced for sputtering and condensation at a pressure of about 0.06 mbar. Under these initial conditions the cluster deposition rate turned out rather low (Fig. 4.7a)), so other tests were performed at higher Ar pressures of 0.3 mbar, and, consequently, a reduced voltage of ~170 V in order to maintain the same plasma current of 0.50 A. These measures were quite effective to increase the yield, even more so when the setpoint current was raised to 1.00 A (see also Fig. 2.4 in Ch. 2). Coatings that were visible to the eye, and purple in color, were produced in about 20 min deposition time. Addition of helium gas to the aggregation chamber only resulted in smaller clusters, without any noticeable effect on deposition rate.

An interesting side-effect of evaporating niobium was a considerable drop in background pressure. While the system base pressure was typically 2×10^{-8} mbar, it would be an order of magnitude lower immediately after deposition (2×10^{-9} mbar), and then slowly increase again to the normal level. Indeed, one application of Nb is as a getter in vacuum tubes, i.e., as a substance to remove trace amounts of other substances by chemical combination.

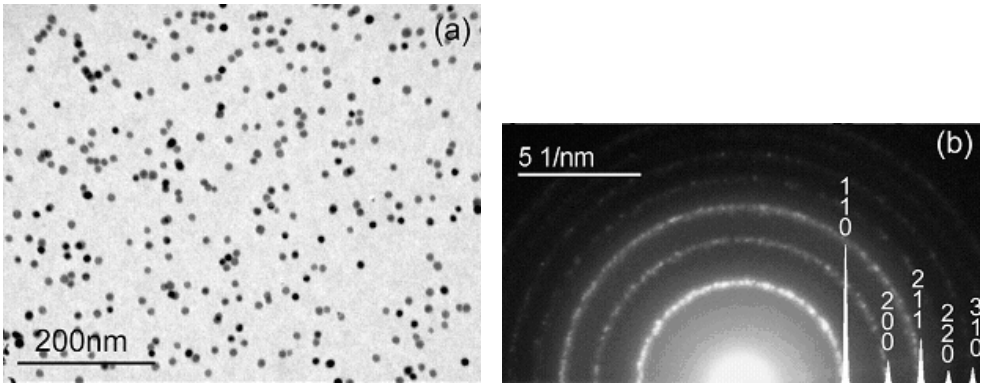

Figure 4.7: (a) *TEM bright field image of Nb nanoclusters on Si_3N_4 after 10 min deposition;* **(b)** *Selected area diffraction profile of the as-deposited film; simulated peaks for bcc niobium are superimposed.*

Figure 4.7(a) is a typical TEM bright-field image of niobium clusters supported on Si_3N_4, obtained after 10 min deposition. The particles with an average diameter of about 10 nm are randomly dispersed, as it was also observed by AFM on Si substrates. Selected-area diffraction was performed on the as-deposited film,

confirming that the clusters have a bcc crystal structure (Fig. 4.7(b)). Contrary to the case of iron, the niobium clusters do not possess any oxide shell. The clusters are relatively stable under irradiation with the electron beam, which makes them reasonably easy to analyze by TEM compared to other elements that frequently suffer from structural instability. The latter is illustrated for an iron cluster in Figure 4.2(c).

In a <111> projection, a Nb cluster clearly demonstrates a hexagonal shape as seen in Fig. 4.8. Combined with observations of hexagonal <110> and square <100> projections, this suggests that the crystal habit at room temperature is a rhombic dodecahedron. Therefore the truncation ratio λ_2/λ_1 would be equal to zero, as explained in the previous section. Using the relation $\lambda_2/\lambda_1 = 2-\sqrt{2}\left(\gamma_{100}/\gamma_{110}\right)$ based on the Wulff construction (Eq. 4.3), we find a ratio of surface energies $\gamma_{100}/\gamma_{110} \geq \sqrt{2}$. This agrees with the fact that {110} planes generally have the lowest surface energy for bcc structures, although calculations [7] have actually indicated the reverse for niobium ($\gamma_{100}/\gamma_{110} \approx 0.93$).

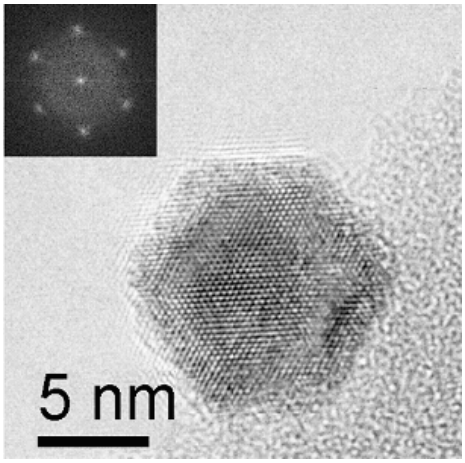

Figure 4.8: *A single Nb nanocluster as-deposited on a Si_3N_4 substrate. Inset shows the power spectrum.*

Annealing treatments were performed *in situ* to a maximum temperature of 800-900°C. According to the supplier of the Si_3N_4 membranes (SPI), they should be stable up to 1000°C, but our experience has shown that the maximum temperature is closer to 900°C. However, the main reason to stop the treatment between 800°C and 900°C is for protection of the microscope. Considerable transformations of the Nb clusters occur at these elevated temperatures, as evident from diffraction analysis in Figure

4.9. Structural changes first become apparent around 300ºC, from a slight shift of the 110 peak. The maximum shift is observed around 500ºC, where it represents an increase in lattice parameter of approximately 7%. Such an expansion marks the initial stage of the bcc to fcc structural transformation, which is completed at 800ºC.

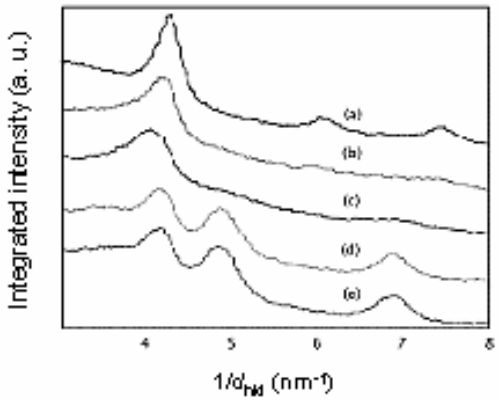

Figure 4.9: *Integrated intensity of the diffraction profile in the range 3 – 8 nm^{-1} as it develops during in-situ heat treatment:* ***(a)*** *as–deposited,* ***(b)*** *300 ℃,* ***(c)*** *500 ℃,* ***(d)*** *800 ℃,* ***(e)*** *slowly cooled to RT. First, the shift and broadening of the peak is visible, then, the fcc structure appears and remains unaltered upon cooling.*

The observed changes are due to oxidation of the clusters. The oxide phase is, with high probability, cubic monoxide (NbO) as this is known to form under low oxygen pressures [8] such as those in the TEM (ambient vacuum of ~10^{-4} mbar during *in situ* heating). Electron energy loss spectroscopy (EELS) performed after annealing clearly revealed the presence of oxygen in the analyzed area, confirming the formation of niobium oxide.

More detailed information is provided by lattice imaging as in Figure 4.10(a), which shows the same cluster as displayed in Figure 4.8 after a heat treatment at 800°C. Splitting and shifting of the originally 110_{bcc} spots is visible in the enlarged power spectrum of Figure 4.10(b). The measured proportion of the split spots is determined to be 1.145, in good agreement with the theoretical value for an fcc lattice d_{111}/d_{200}=1.155. These observations indicate the formation of niobium oxide subdomains of various 110 orientations within the nanocluster, rather than an oxide monocrystal of $<110>_{fcc}$ orientation. The structure obtained by heating remains unaltered when the sample is slowly cooled down to room temperature.

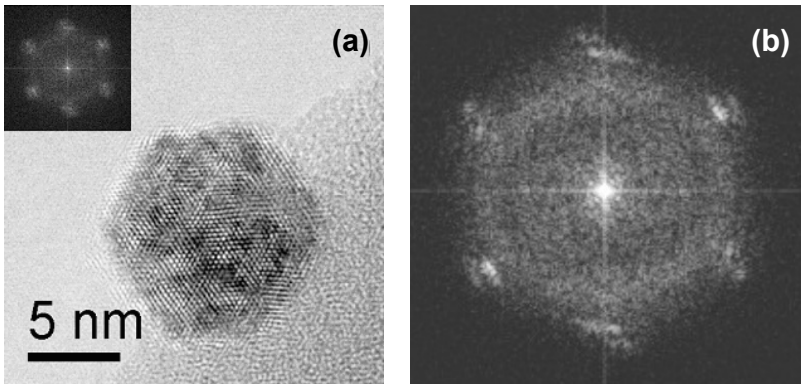

Figure 4.10: (a) *The same cluster as depicted in Fig. 4.8, after heating to ~800℃.* **(b)** *Enlarged view of the power spectrum showing splitting and shifting of spots.*

When comparing the cluster before and after heating in Figures 4.8 and 4.10(a), we do not observe any significant change in size. For Nb and NbO phases, the volumes per atom are 1.81×10^{-2} nm^3 and 2.54×10^{-2} nm^3, respectively. Even if the entire cluster was oxidized and converted to NbO, this would lead to a cluster size ratio d(NbO)/d(Nb)≈1.12, i.e., an increment of at most 12%. Theoretically such a small difference could be observed by TEM, although the delocalization effect around cluster edges might hinder an accurate observation. Image delocalization occurs when a detail in the image is displaced relative to its true location in the specimen. A characteristic of a field-emission gun TEM such as the JEOL 2010F is that single features are imaged as peaks having adjacent submaxima of decreasing intensity (the point spread function). While this may not affect the visualization of the periodic structure within a particle, fringes from the particle can appear outside of it [9].

Niobium clusters remain as separate entities (Fig. 4.11) even at the highest annealing temperatures (800°C), nearly one third the melting temperature of bulk Nb (T_m=2468°C; 1937°C for NbO). Depending on feature size, the melting temperatures of nanometer scale structures are generally lower than for the solid, but since no coalescence was observed in the present case, the Nb clusters are likely to have a melting point close to the bulk value. The particles clearly have faceted shapes which can further explain the absence of coalescence, as pointed out earlier in sections 3.1 and 3.4. Where facets are present the local curvature is zero, and thus the driving force for atoms to migrate is removed. Coalescence is then determined by the nucleation rate of defects on the facets. Also, the edges formed by facets can act as barriers to atomic diffusion [10].

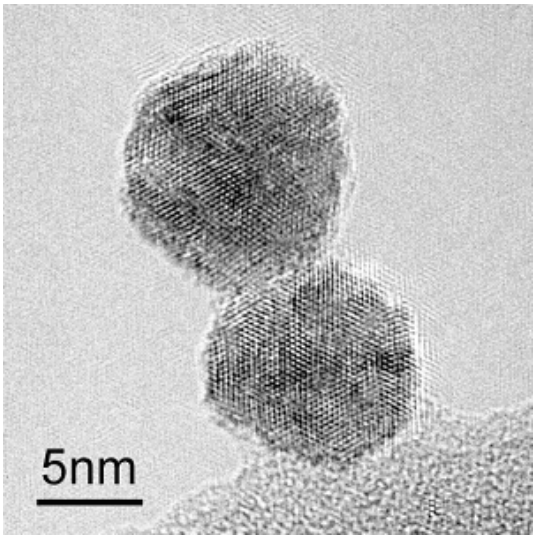

Figure 4.11: *Two Nb nanoclusters after heat treatment at 800°C.*

Summarizing, the niobium clusters do not develop an oxide shell under atmospheric conditions contrary to the case of iron. Oxidation only occurs during heating, where the clusters oxidize internally under high vacuum, forming NbO subgrains with an fcc structure. Coalescence of clusters at elevated temperatures (T_{max}~800°C) was not observed, probably due to the faceted shape of clusters and the high barrier for nucleation of defects on the facets. Previous suggestions in the literature that Nb nanoclusters should have a truncated rhombic dodecahedral habit [2] were not confirmed by our TEM observations. In fact, the degree of truncation was zero indicating that the {110} faces have significantly lower surface energy than {100} faces.

4.4 Size-dependent structure and self-assembly of molybdenum clusters

Molybdenum nanoclusters were generated by operating the deposition source with a fixed ion current of 0.25 A, and a corresponding voltage of 200-250 V (~55 W). The base pressure in the system was of the order of 10^{-7} mbar. The aggregation zone was filled with argon to a pressure of 0.15 mbar. Clusters produced under these conditions, and with an intermediate aggregation length, were about 5 nm in size. Due to the interesting size-dependent effects for Mo clusters, it was desirable to form both smaller and larger particles. Through an increase in the aggregation length by +50 mm, an average cluster size of about 9 nm was achieved. On the other hand, small clusters were most easily formed by adding helium as a drift gas, to a combined pressure of 0.7 mbar, and keeping other conditions the same. The resulting Mo clusters were about 2.5 nm in size. Addition of helium also decreases the deposition rate, extending the time needed to form a monolayer to more than 5 min.

As-deposited molybdenum clusters with a diameter larger than 4 nm were found to have a body centered (bcc) crystal structure. In contrast, for smaller clusters the atoms are ordered in a face centered (fcc) arrangement. Fourier transform measurements on the latter (Fig. 4.12) indicated lattice spacings of 0.213 nm for the (200) planes and 0.242 nm for the (111) planes. The ratio of these spacings is 1.14, which is very close to the theoretical value for an fcc lattice $2/\sqrt{3}$ ($\cong$1.15). Our observations suggest that a structural transition between fcc and bcc occurs for a cluster size around 3 nm. Previously [3], this has been shown to take place for nanoclusters of 1460-3900 atoms, or, equivalently, 3.6-5.0 nm diameter. Electron diffraction and electron energy loss spectroscopy measurements showed that neither the bcc nor fcc clusters contain any oxide, despite a brief exposure to atmosphere during sample transfer.

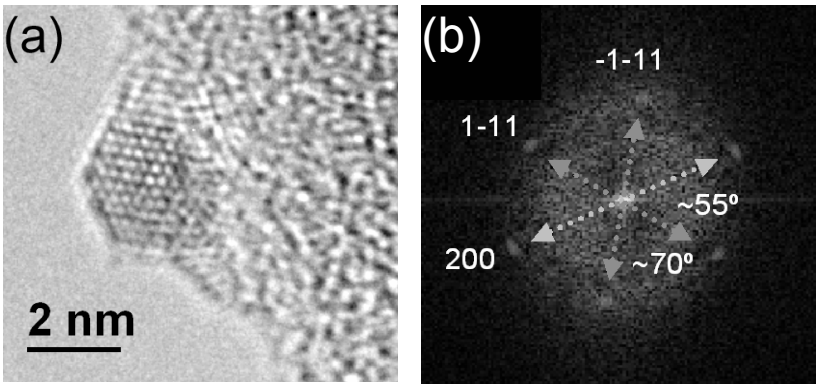

Figure 4.12: (a) *TEM image of a small Mo cluster approximately 2.5 nm in size.* **(b)** *Characteristic angles of an fcc structure in the power spectrum.*

An intriguing aspect of the larger Mo clusters is their apparently square shape, as seen in Figure 4.13. Deposited cubic Mo particles with a size of 5 nm have been observed before by TEM [11,12]. For a cubic particle, the condition $\gamma_{100}/\gamma_{110} \leq 1/\sqrt{2}$ should be satisfied if the Wulff construction applies. However, calculations [7] for bcc Mo have indicated rather different ratios for the surface energies of (100) and (110) planes, with $\gamma_{100}/\gamma_{110} \approx 1.12$. The latter is between $1/\sqrt{2}$ and $\sqrt{2}$, which would favor a truncated rhombic dodecahedral habit [2]. Nevertheless, the crystal habit can also be determined by kinetics, so that a particle will be cubic if the (100) facets grow faster than the (110) facets.

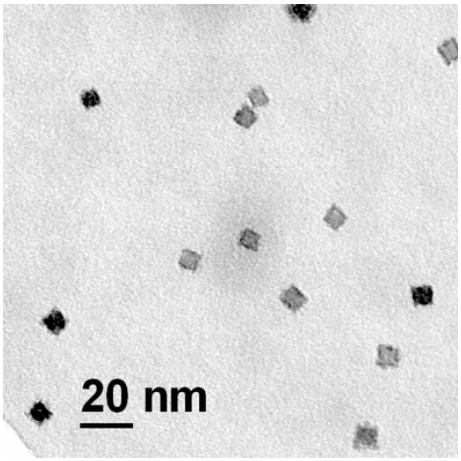

Figure 4.13: *TEM bright field picture of Mo nanoclusters deposited onto Si_3N_4. Cluster size≈5 nm.*

Apart from the possibility that the particles are cubes, their square shape in TEM images could also be the two-dimensional projection of a cuboctahedron. This was further investigated by recording the phase change of an object wave by electron holography, a technique that has been successfully applied in the analysis of nanoparticle shapes [13]. The essence of electron holography is the combination of two beams within the microscope: the incident, undeviated electron beam and the image beam, which exits the bottom surface of the thin specimen. If the electron optical geometry is correctly set up, these two beams can be made to interfere. The interference pattern is then processed using optical techniques to form a hologram, allowing the separation of phase components in the TEM image from amplitude components. In the absence of any electric and magnetic field in the sample and neglecting dynamical diffraction effects [14], the phase change is given by

$\Delta\Phi = C_E \times V_0 \times t$. Here, the constant C_E is equal to 7.28×10^6 $m^{-1}eV^{-1}$ for 200 kV electrons, V_0 is the mean inner crystal potential in units of eV, and t is the object thickness measured in meters. The phase change is therefore linearly dependent on object thickness. A reconstructed phase signal is shown in Figure 4.14, where the phase in the projected object was reconstructed from holograms acquired in several orientations close to the <100> zone axis, in order to minimize dynamical diffraction effects. The nearly constant phase implies a more or less constant object thickness, so that a cuboctahedral crystal habit can be excluded.

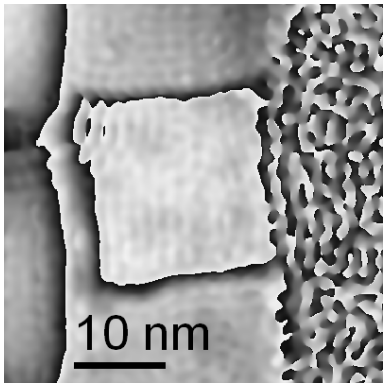

Figure 4.14: *Phase change within a Mo cluster of size 20 nm resting on a Si_3N_4 membrane, reconstructed from an electron hologram demonstrating nearly constant thickness in the projected direction. The hologram, taken at a biprism voltage adjusted to give 0.5 nm fringes, was recorded on a 1k×1k Gatan multiscan 794IF CCD camera. The phase was reconstructed using the HoloWorks software package.*

Previous studies [11,12] have shown that 5 nm cubes of Mo self-assemble into larger particles, leading to the formation of cubes consisting of 2×2×2, 3×3×3, or 4×4×4 smaller structural units. The self-organization process probably occurs to decrease the surface energy of the system [2]. On closer inspection of our Mo clusters, the cubes have rather distorted wavy edges (Fig. 4.15(a)) so that the term cuboids is more appropriate. This suggests a self-assembly from building blocks other than cubes, or alternatively, an imperfect arrangement of subunits. The latter is unlikely because it would not yield a significant decrease in surface energy. Instead, the unit particle that forms the building block of the larger cuboids could be a rhombic dodecahedron; this would also explain the ledges along the particle sides as seen in Figure 4.15(a). Large self-assembled cuboids about 30 nm in size were occasionally observed in the samples with small Mo clusters ($D \leq 4$ nm, Fig. 4.15(b)). Here, the small particles visible in the background are not cubic which also suggests that Mo cuboids are constructed from subunits of a different shape.

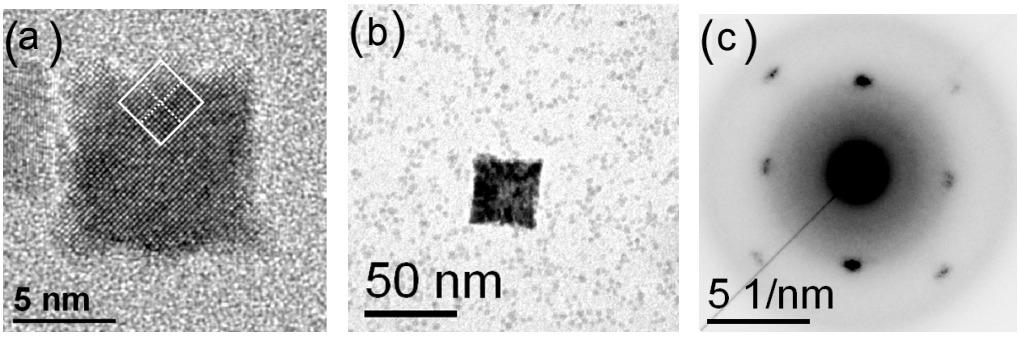

Figure 4.15: (a) *HRTEM image along a <100> direction; projection of a rhombic dodecahedron is superimposed.* **(b)** *Large cuboidally shaped particle surrounded by non-cubic small clusters of size ~4 nm.* **(c)** *Selected area electron diffraction from the large cuboid in (c); splitting of (110) peaks due to self-assembly.*

Annealing leads to a change in morphology of the molybdenum clusters, in the same way as described for iron. Coalescence was observed at temperatures around 800°C, which is less than 1/3 the melting temperature of bulk Mo (2623°C). Fusion processes are not hindered by a molybdenum oxide phase although the influence from facets is still present. Figure 4.16 illustrates the situation after annealing, where the rounded shape of the large particle is reminiscent of a truncated rhombic dodecahedron, albeit with rounded facet corners. After coalescence, truncation of the initially cuboidal shape probably becomes favorable, i.e., {100} becomes more stable, leading to the observed rounded shape.

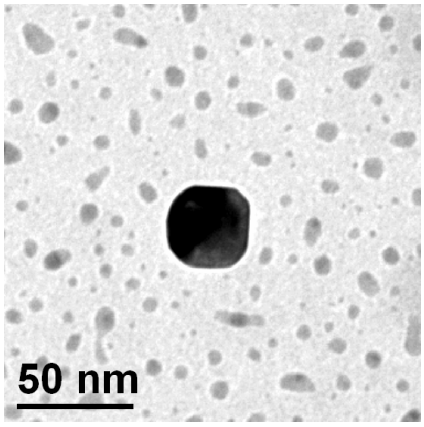

Figure 4.16: *TEM image of a large Mo particle surrounded by smaller clusters after annealing at 800℃.*

In summary, our observations confirm that the crystal structure of Mo clusters is size-dependent. The bulk bcc phase is stable for clusters of 4 nm diameter or larger, while the fcc phase appears in clusters with a size ≤3 nm; both are oxide-free. The reason for the size dependence is that the fcc structure is more compact than bcc, and provides a lower surface energy which becomes the critical factor below a certain size. On the other hand, the bcc structure has stronger bonding which yields an energy gain above the critical cluster size [3]. The larger Mo clusters have a cuboidal shape and appear to be self-assembled from smaller structural units. We have identified the rhombic dodecahedron as the most likely shape for these subunits. Self-organization into large cuboids was also observed for the smaller (fcc) Mo clusters. Annealing of clusters results in coalescence around 800°C, and a transformation of initially cuboid particles to truncated rhombic dodecahedra.

References

1. P. Melinon, V. Paillard, V. Dupuis, A. Perez, P. Jensen, A. Hoareau, J. P. Perez, J. Tuaillon, M. Broyer, J. L. Vialle, *et al.*, *From free clusters to cluster-assembled materials.* Int. J. of Mod. Phys. **9**, 339 (1995).
2. A. S. Edelstein and R. C. Cammarata, *Nanomaterials: synthesis, properties and applications* (Institute of Physics Publishing, Bristol and Philadelphia, 1996).
3. S. H. Huh, H. K. Kim, J. W. Park, and G. H. Lee, *Critical cluster size of metallic Cr and Mo nanoclusters.* Phys. Rev. B **62**, 2937 (2000).
4. M. D. Upward, B. N. Cotier, P. Moriarty, P. H. Beton, S. H. Baker, C. Binns, and K. Edmonds, *Deposition of Fe clusters on Si surfaces.* J. Vac. Sci. Techn. B **18**, 2646 (2000).
5. V. Dupuis, J. P. Perez, J. Tuaillon, V. Paillard, P. Melinon, A. Perez, B. Barbara, LThomas, S. Fayeulle, and J. M. Gay, *Magnetic properties of nanostructured thin films of transition metal obtained by low energy cluster beam deposition.* J. Appl. Phys. **76**, 6676 (1994).
6. N. A. Besley, R. L. Johnston, A. J. Stace, and J. Uppenbrink, *Theoretical study of the structures and stabilities of iron clusters.* J. of Molec. Struct. (THEO CHEM) **341**, 75 (1995).
7. Q. Jiang, H. M. Lu, and M. Zhao, *Modelling of surface energies of elemental crystals.* J. Phys.: Condens. Matter **16**, 521 (2004).
8. M. Petrucci, C. W. Pitt, S. R. Reynolds, H. J. Milledge, M. J. Mendelssohn, C. Dineen, and W. G. Freeman, *Growth of thin-film niobium and niobium oxide layers by molecular-beam epitaxy.* J. Appl. Phys. **63**, 900 (1988).
9. D. B. Williams and C. B. Carter, *Transmission electron microsopy III: Imaging in the TEM* (Plenum Press, New York, 1996).
10. P. Jensen, *Growth of nanostructures by cluster deposition: Experiments and simple models.* Rev. Mod. Phys. **71**, 1695 (1999).
11. A. S. Edelstein, G. M. Chow, E. I. Altman, R. J. Colton, and D. M. Hwang, *Self- arrangement of molybdenum particles into cubes.* Science **251**, 1590 (1991).
12. F. H. Kaatz, G. M. Chow, and A. S. Edelstein, *Narrowing sputtered nanoparticle size distributions.* J. Mat. Res. **8**, 995 (1993).
13. L. F. Allard, E. Voelkl, A. Carim, A. K. Datye, and R. Ruoff, *Morphology and crystallography of nanoparticulates revealed by electron holography.* Nanostruct. Mater. **7**, 137 (1996).
14. J. Li, M. R. McCartney, and D. J. Smith, *Semiconductor dopant profiling by off-axis electron holography.* Ultramicroscopy **94**, 149 (2003).